ACS NANO
Cite This: ACS Nano 2018, 12, 3646−3657
www.acsnano.org

ARTICLE

Rupture of Lipid Membranes Induced by Amphiphilic Janus Nanoparticles

Kwahun Lee,[†] Liuyang Zhang,[‡] Yi Yi,[†] Xianqiao Wang,[§] and Yan Yu*[,†]

[†]Department of Chemistry, Indiana University, Bloomington, Indiana 47405, United States
[‡]State Key Laboratory for Manufacturing Systems Engineering, Xi'an Jiaotong University, Xi'an, Shaanxi 710049, China
[§]College of Engineering, University of Georgia, Athens, Georgia 30602, United States

Supporting Information

ABSTRACT: The surface coatings of nanoparticles determine their interaction with biomembranes, but studies have been limited almost exclusively to nanoparticles with a uniform surface chemistry. Although nanoparticles are increasingly made with complex surface chemistries to achieve multifunctionalities, our understanding of how a heterogeneous surface coating affects particle−biomembrane interaction has been lagging far behind. Here we report an investigation of this question in an experimental system consisting of amphiphilic "two-faced" Janus nanoparticles and supported lipid membranes. We show that amphiphilic Janus nanoparticles at picomolar concentrations induce defects in zwitterionic lipid bilayers. In addition to revealing the various effects of hydrophobicity and charge in particle−bilayer interactions, we demonstrate that the Janus geometry—the spatial segregation of hydrophobicity and charges on particle surface—causes nanoparticles to bind more strongly to bilayers and induce defects more effectively than particles with uniformly mixed surface functionalities. We combine experiments with computational simulation to further elucidate how amphiphilic Janus nanoparticles extract lipids to rupture intact lipid bilayers. This study provides direct evidence that the spatial arrangement of surface functionalities on a nanoparticle, rather than just its overall surface chemistry, plays a crucial role in determining how it interacts with biological membranes.

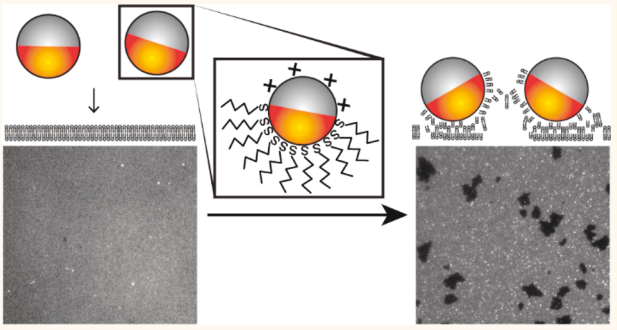

KEYWORDS: *nanoparticles, amphiphilic, Janus particles, lipid bilayer, membrane defects, particle−membrane interaction*

To predict the impact of synthetic nanoparticles on living systems, it is essential to understand how they interact with biological membranes. Exploring the role that particle surface coatings have on these interactions is of central importance. For particles with uniform surface chemistry, surface properties such as charge,[1−8] hydrophobicity,[8−13] and adsorbed protein corona[14−19] have been shown to play pivotal roles in determining their interaction with biomembranes. Much less is known about the effects of heterogeneous surface chemistry. It has been shown that when the surfaces of hydrophobic polymeric particles (28−140 nm in diameter) are sparsely decorated with anionic groups, they induce the formation of pores in model lipid membranes.[9,20] Gold nanoparticles coated with a mixture of hydrophobic and hydrophilic molecules are capable of stabilizing the open edge of model lipid membranes.[21] These few studies demonstrate that an amphiphilic surface coating alters the interaction of nanoparticles with biomembranes. But, these findings are limited to cases where hydrophobic and charged groups are mixed randomly on the surfaces of particles. Little is known about the effect of a nonuniform spatial arrangement of functional groups on nanoparticle surfaces. Computer simulation studies indicate that such an effect will be significant. They predict that amphiphilic nanoparticles of a few nanometers in size will disrupt lipid membranes *via* different mechanisms depending on the spatial patterns of molecules on their surfaces.[22−29] However, experimental data to support the simulation predictions remain scarce. One experimental study claimed that gold nanoparticles with striped patterns of hydrophobic and hydrophilic molecules penetrate cell membranes more easily than randomly patterned ones,[30,31] but confirmation of the "stripy" surface morphology has been called into question.[32−34] An understanding of the interaction between nanoparticles with heterogeneous surface chemistries and biological membranes is still lacking. This knowledge is becoming more critical, as nanoparticles are increasingly engineered to possess complex surface coatings in order to achieve more sophisticated functions.

Received: January 29, 2018
Accepted: April 4, 2018
Published: April 4, 2018

DOI: 10.1021/acsnano.8b00759
ACS Nano 2018, 12, 3646−3657

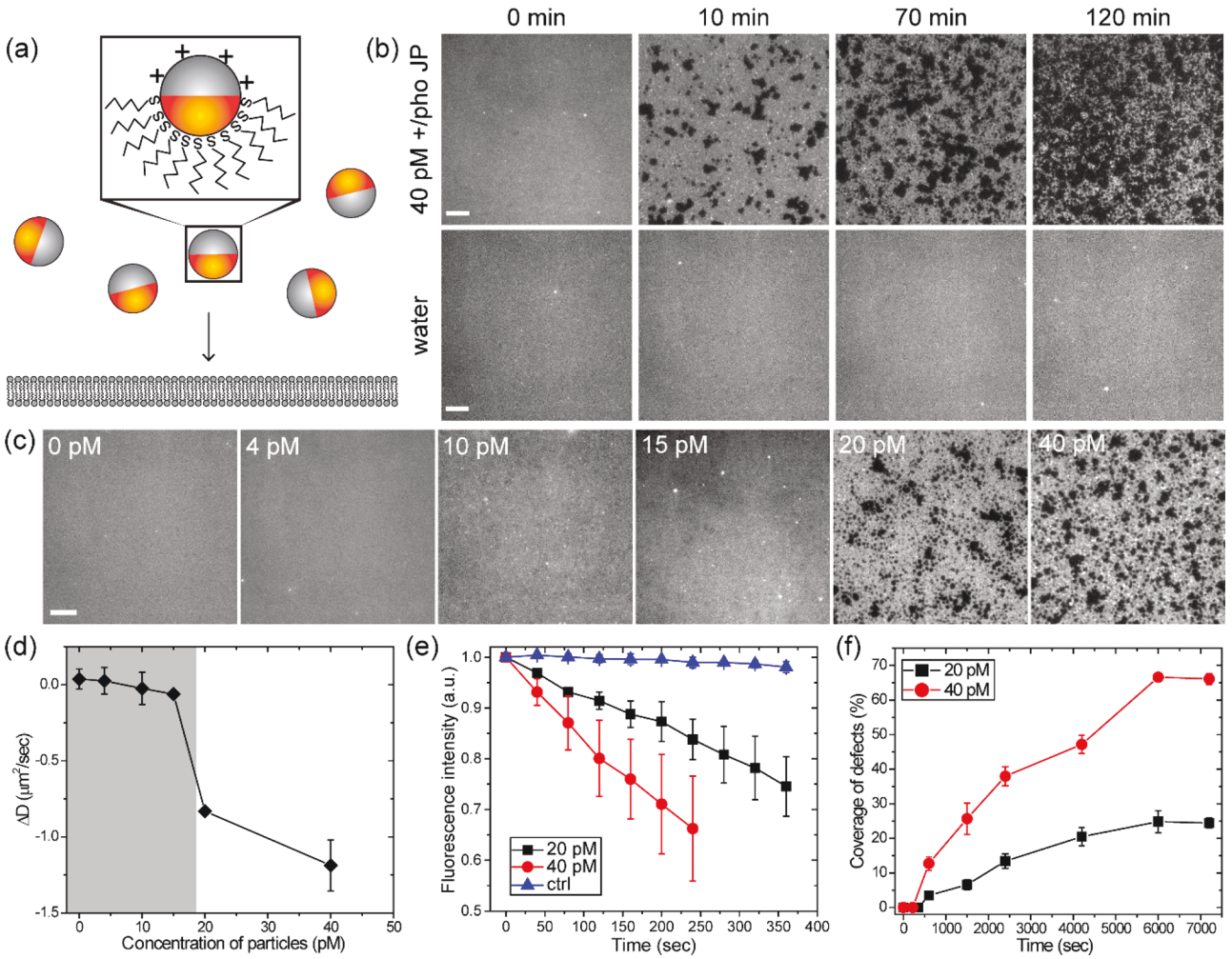

Figure 1. Disruption of the supported DOPC lipid bilayer induced by +/pho JPs. (a) Schematic illustration of the experimental system (orange represents the hydrophobic side; gray represents the cationic side). (b) Fluorescence images showing the morphology of bilayers as a function of time in the presence of 40 pM +/pho JPs (top) and in water without particles (bottom). (c) Fluorescence images showing the morphology of the bilayers at 70 min after interaction with +/Pho JPs at various concentrations. (d) Change in lipid diffusion coefficient (ΔD) after the addition of water (0 pM) or +/pho JPs at various concentrations. (e) Average fluorescence intensity of bilayers as a function of time after the addition of water (blue) or +/pho JPs at 20 pM (black) and 40 pM (red). After the formation of defects, only areas free of defects were measured. (f) Surface coverage of defects in bilayers as a function of time in the presence of 20 pM (red) or 40 pM (black) +/pho JPs. Scale bars: 10 μm

Here we investigate this problem using an experimental system consisting of amphiphilic "two-faced" Janus nanoparticles and supported lipid membranes. The Janus particles, 100 nm in diameter, are hydrophobic on one hemisphere and charged on the other. The well-defined anisotropic distribution of functional groups on the surfaces of Janus particles allowed us to quantitatively explore the connection between the way in which surface chemistry is spatially organized and particle–membrane interactions. We showed that amphiphilic Janus nanoparticles at picomolar (pM) concentrations induced defects in zwitterionic lipid bilayers, whereas particles that were coated uniformly with hydrophobic and charged molecules did not. We distinguished the effects of hydrophobicity, charge, and Janus geometry on particle–membrane interactions by combining super-resolution fluorescence microscopy, measurements of the orientation of single Janus nanoparticles, and quantification of particle–membrane binding affinity. The pathway by which amphiphilic Janus nanoparticles caused defects in intact lipid bilayers was further elucidated by computer simulation. Our results demonstrate that the spatial segregation of hydrophobic and charged groups on Janus nanoparticles enhances their ability to disrupt lipid membranes over that of other amphiphilic nanoparticles. These findings indicate that, besides the overall surface chemistry of nanoparticles, the spatial arrangement of this surface chemistry is vital to assessing their biological effects.

RESULTS AND DISCUSSION

Our experimental system consisted of 1,2-dioleoyl-*sn*-glycero-3-phosphocholine (DOPC) lipid bilayers formed on glass substrates and 100 nm amphiphilic Janus nanoparticles in deionized water (Figure 1a). The cationic/hydrophobic Janus nanoparticles (referred to as +/pho JPs) were prepared by depositing a thin gold layer of 25 nm thickness onto one hemisphere of amine-functionalized silica nanoparticles and then conjugating octadecanethiol (ODT) on the gold caps (Figure S1a). The resulting Janus nanoparticles were hydrophobic on one hemisphere and positively charged on the other with a surface charge density of ~2 amine groups/nm^2. Similar procedures were used for preparing anionic/hydrophobic

DOI: 10.1021/acsnano.8b00759
ACS Nano 2018, 12, 3646–3657

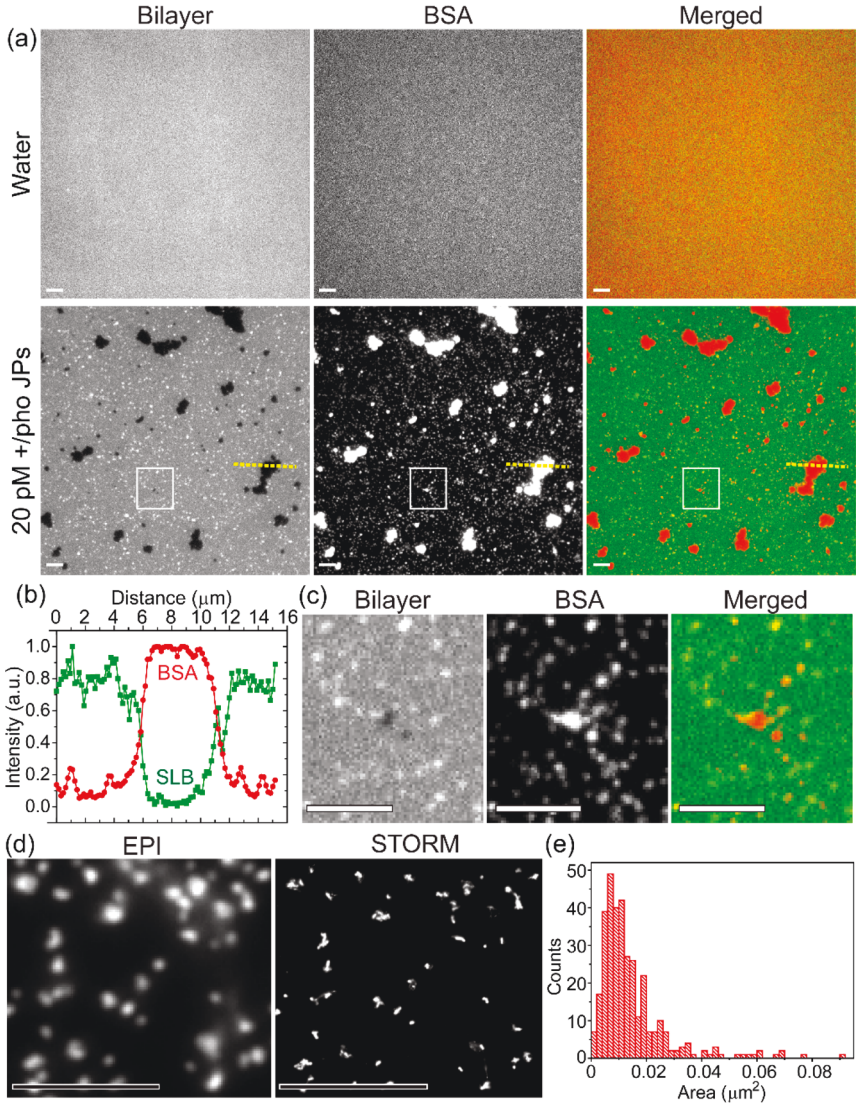

Figure 2. Quantification of defects in lipid bilayer. (a) Fluorescence images showing the lipid bilayer and fluorescently labeled BSA adsorbed on the bilayer in the presence of water (top) or 20 pM +/pho JPs. (b) Fluorescence line-scan profile of the lipid bilayer and BSA of a defect (marked with yellow dashed lines in (a)). (c) Zoomed-in images of a representative region (marked with white rectangular boxes in (a)) showing the adsorption of BSA in the bilayer defects and on small lipid aggregates. (d) Images from epi-fluorescence microscopy (EPI) and stochastic optical reconstruction microscopy (STORM) showing BSA-Alexa 647 adsorbed on small lipid aggregates. (e) Histogram showing the domain size of the small lipid aggregates, measured from STORM images. The average domain size is 1.55×10^{-2} μm^2 ($N = 344$). Scale bars: 5 μm.

(−/pho JPs) and dipolar Janus particles (+/− JPs). Both types of particles display carboxylic acid groups on their anionic hemisphere. The anisotropic surface chemistry of these amphiphilic nanoparticles was confirmed by their phase transfer behavior at the toluene/water interface and their morphology in scanning electron microscopy (SEM) (Figure S1b,c). The ζ-potential for bare amine silica nanoparticles was +25.9 mV in deionized water, indicating that the amine groups were indeed positively charged under the experimental condition. It decreased to −3.2 mV after the deposition of a gold layer on one hemisphere of the particles. This decrease in ζ-potential reflects, in part, the reduced number of amine groups after gold coating. But more importantly, it is likely an effect from the unusual electrokinetic motion of metal-coated Janus particles, which does not obey the classical electrophoretic models used in ζ-potential measurements.[35] After functionalization of the hydrophobic coating, ζ-potentials of +/pho and −/pho JPs were −15.7 and −24.4 mV, respectively (Figure S2).

We first investigated how the morphology of lipid bilayers changed with time after their interaction with 40 pM +/pho JPs (Figure 1b). Small lipid aggregates and μm-sized defects that were depleted of fluorescent lipids appeared on the bilayers within 10 min after the nanoparticles were added. Both the number of lipid aggregates and the size of the defects increased with time. At the same time, the overall fluorescence intensity of the remaining bilayer gradually decreased, suggesting a loss of lipids. In the absence of the +/pho JPs, bilayers remained unchanged for over 2 h of observation, confirming that the formation of lipid aggregates and defects is caused by the addition of +/pho JPs. To determine the threshold concentration of particles needed to trigger this disruption of the bilayers, we varied the concentration of +/pho JPs from 0 to 40 pM and examined the bilayers 70 min after they were

DOI: 10.1021/acsnano.8b00759
ACS Nano 2018, 12, 3646−3657

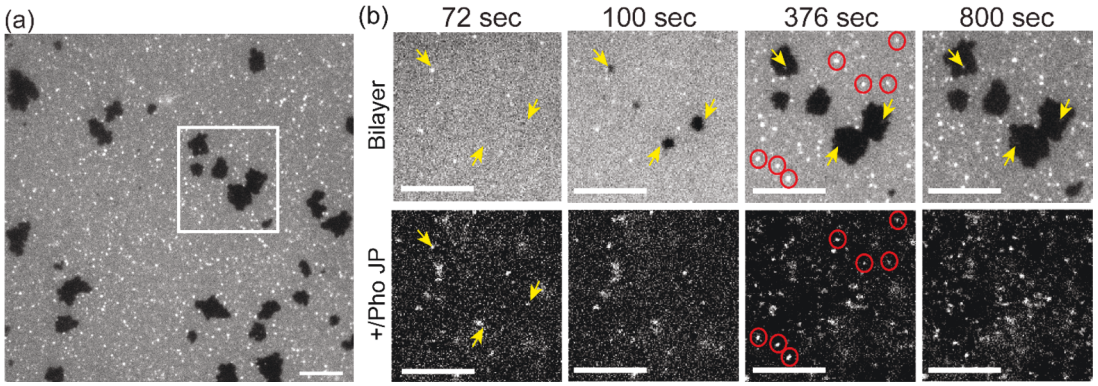

Figure 3. Dual-color fluorescence imaging of +/pho JPs and the lipid bilayer. Approximately 25% of the particles were fluorescently labeled. (a) Fluorescence image showing the formation of lipid aggregates and defects after the addition of 20 pM +/pho JPs. (b) Zoomed-in images of a representative region as marked in (a). Yellow arrows indicate locations where defects were formed and propagated. Red circles indicate the colocalization of +/pho JPs with small lipid aggregates. Scale bars: 10 μm.

incubated with the particles (Figure 1c). No obvious changes occurred when particle concentrations were 4 pM or lower. As particle concentration was increased to 10 pM, small lipid aggregates started to appear on the bilayers. However, defects only began to appear at particle concentrations of 20 pM and higher. The same concentration dependence was observed for changes in membrane fluidity. Lipid diffusion coefficient was measured using fluorescence recovery after photobleaching (FRAP). Bilayers remained fluidic at particle concentrations of 15 pM or lower, as indicated by the only slight decrease in lipid diffusion coefficient (Figure 1d). However, lipid diffusion decreased drastically at a particle concentration of 20 pM, when large defects in bilayers also became visible. Beyond this threshold concentration, higher particle concentrations sped up their disruption to the bilayer, as indicated by a faster decrease in the fluorescence intensity of the remaining lipid bilayer as well as a faster progression of the defects (Figure 1e,f). Interestingly, the overall surface coverage of defects reached a steady plateau stage after approximately 2 h. It is important to note that measurements of bilayer fluorescence intensity were done only for the early time points, because later the area of the defects became too large to allow accurate measurements of lipid diffusion in remaining intact areas of the bilayer. The results together demonstrate that +/pho JPs at concentrations of 20 pM or higher disrupt DOPC lipid bilayers in a manner that is dependent on particle concentration and time.

The defects seen in bilayers might be holes in the membrane, but they might also be gel-phase domains from which bulky fluorescent lipid markers were excluded. To determine the nature of the defects, we performed two sets of experiments. In the first set, we tested the effect of temperature on the defects. This is because gel-phase lipid domains should disappear at higher temperatures, but holes in bilayers should not. After defects were formed with 20 pM +/pho JPs, we gradually increased the temperature of the bilayer. Defects in the bilayer remained unchanged even at 57 °C, a temperature at which most lipids are expected to be in the liquid phase (Figure S3). This is evidence that the observed defects are holes and not gel-phase lipid domains. In the second set of experiments, we added fluorescent bovine serum albumin (BSA) to the bilayers after the defects were visible. BSA, commonly used for surface passivation, is known to adsorb strongly on bare glass surfaces but not on zwitterionic lipid bilayers. It would thus label holes where glass surface was exposed.[36,37] In our experiments, BSA was observed to selectively fill all the defects at 20 pM +/pho JPs, with negligible adsorption on the lipid bilayer (Figure 2a,b). This result again confirms that the defects are indeed holes depleted of lipids. When the defects were labeled by fluorescent BSA, we were able to resolve smaller nanosized defects, which were likely formed prior to the appearance of larger ones. BSA was also found to colocalize with the small lipid aggregates (Figure 2c). By using stochastic optical reconstruction microscopy (STORM) and BSA labeled with the STORM-suitable dye Alexa 647, we determined the cross-sectional area of those lipid aggregates to be 4.54×10^{-4} to 1.55×10^{-1} μm^2 with an average of 1.55×10^{-2} μm^2 per aggregate ($N = 344$) (Figure 2d,e). This indicates an average size of ~120 nm for the lipid aggregates, assuming they are spherical.

BSA does not adsorb on lipid bilayers but does adsorb strongly on bare +/pho JPs (Figure S4 SI). Thus, the observation of BSA adsorption onto lipid aggregates raised the question of whether those aggregates contain exposed Janus particles. To answer this question, we fluorescently labeled the +/pho JPs and imaged both the particles and the bilayer during their interaction at 20 pM concentrations of particles. We kept the dye labeling efficiency low to minimize possible alteration to the cationic charges of the particles. To allow the resolution of single particles in imaging, fluorescent +/pho JPs were mixed with nonfluorescent ones at a 1:3 ratio. As shown in Figure 3 and Movie S1, +/pho JPs first adsorbed on lipid bilayers, and then, within tens of seconds, small lipid aggregates formed at the same locations. This indicates that lipid–particle complexes formed following the initial contact between +/pho JPs and the bilayer. As more +/pho JPs became adsorbed on the bilayer, defects started to appear at the locations of some lipid–particle complexes (indicated by the yellow arrows) and then propagated to become larger ones. Near some other lipid–particle complexes (indicated by red circles) no defects were visible within the resolution limits of the fluorescence microscopy. These results show that the adsorption of +/pho JPs on the DOPC lipid bilayer led to the extraction of lipids, which formed complexes with the particles. With increasing loss of lipids, defects started to form. The defects started as nanosized ones, as shown by the BSA backfilling results (Figure 2d,e), but progressed into larger ones as more +/pho JPs adsorbed nearby. The observation of BSA adsorption on those lipid–particle complexes suggests that the +/pho JPs contained in the complexes were not entirely covered by lipids but rather

DOI: 10.1021/acsnano.8b00759
ACS Nano 2018, 12, 3646–3657

are partially exposed. This also agrees with our dual-color imaging observation that some +/pho JPs did not colocalize with lipids.

Given their Janus geometry, it is possible that +/pho JPs have a preferred orientation during their interaction with the lipid bilayer. To determine this, we measured the orientation of single particles by making use of their optical anisotropy. Janus particles that are fluorescent on one hemisphere and metal-capped on the other exhibit varying intensities of fluorescence depending on their orientation due to the blocking of light by the opaque gold cap.[38−40] We used this principle to infer the orientations of individual particles after adding 20 pM of +/pho JPs (fluorescently labeled:nonlabeled = 1:3) to a lipid bilayer. The intensity of single fluorescent particles was measured from below the lipid bilayer using an inverted fluorescence microscope. To calibrate the fluorescence intensity at different particle orientations, we adsorbed +/pho JPs on either hydrophilic or hydrophobic *n*-octadecyltrimethoxysilane (OTE)-coated substrates. On the hydrophilic substrate, the +/pho JPs were oriented with their fluorescent cationic hemispheres facing downward, as confirmed in SEM images, and exhibited strong fluorescence (795 ± 74 au) (Figure 4a).

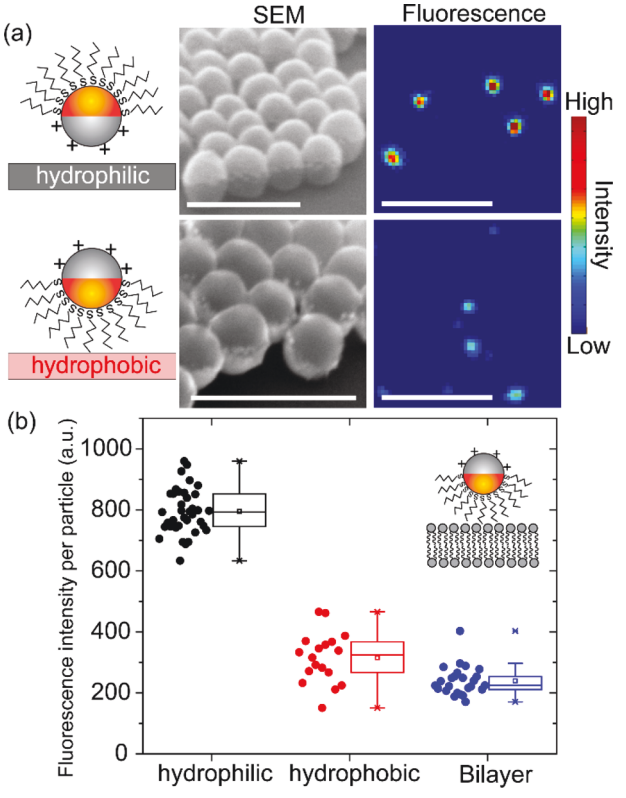

Figure 4. Quantification of the orientation of +/pho JPs on lipid bilayers. The cationic hemisphere of the +/pho JPs was fluorescent and the hydrophobic hemisphere was opaque due to the gold coating. (a) Schematic illustrations, scanning electron microscopy (SEM) images, and epi-fluorescence images showing the orientation and fluorescence profile of +/pho JPs on hydrophilic and hydrophobic substrates. (b) Average fluorescence intensity per particle on different substrates. Each data point in the scattered plot represents measurement from a single particle. Each box plot indicates the mean (squared dot), median (horizontal line), and the interquartile range from 25% to 75% of the corresponding data set. Scale bars: 500 nm (SEM images) and 10 μm (fluorescence images).

Their fluorescence intensity was similar to that of particles without the opaque hemispheric gold coating (Figure S5), an observation further confirming that the fluorescent hemisphere was the one facing the detector. +/Pho JPs placed on hydrophobic substrates were oriented in the opposite direction, with their hydrophobic gold-coated hemispheres facing downward toward the substrate (also the fluorescence detector). The emitted fluorescence was therefore at its weakest due to being maximally blocked by the opaque gold cap (315 ± 81 au). Compared to both calibration standards, +/pho JPs on bilayers emitted a similar level of weak fluorescence (239 ± 47 au) as the ones on hydrophobic substrates (Figure 4b). These results confirm that the hydrophobic (fluorescent) hemisphere of +/pho JPs is in contact with the lipid bilayer after defect formation. We also observed that some +/pho JPs emitted stronger fluorescence upon their initial landing on the bilayer but that their fluorescence decreased within tens of seconds. This observation implies that the +/pho JPs approached the bilayer preferably from the cationic hemisphere and then rotated to the opposite orientation shortly after landing. But it is possible that other factors, such as particles moving out of focus, might also contribute to the decrease in particle fluorescence during particle adsorption onto the bilayer.

The next important set of questions concerns the role of charge, hydrophobicity, and Janus geometry in the bilayer disruption induced by amphiphilic JPs. To determine the charge effect, we fabricated nanoparticles that were hydrophobic on one hemisphere and anionic on the other displaying carboxylic acid groups (Figure S2). The −/pho JPs exhibited some similarities and some differences from +/pho JPs in their interactions with the bilayer (Figure 5a). First, −/pho JPs did not adsorb onto DOPC bilayers. Instead, they remained freely diffusive in the solution. This observation suggests that charges on the JPs affect their initial adsorption onto the bilayer. Cationic charges seem to facilitate the adhesion of particles, while anionic charges do not. Second, −/pho JPs, like +/pho JPs, induced holes in bilayers. But the defects were fractal-like and occurred only at particle concentrations of 150 pM or higher (Figures 5a, S6, and S7). This threshold concentration is nearly 10 times that for +/pho JPs. It is evident that +/pho JPs are more effective in disrupting DOPC bilayers than −/pho JPs. This charge effect seems consistent with previous reports for studies of uniform particles. In these studies, cationic nanoparticles of a broad size range have been found to induce pores in bilayers, while anionic ones do not.[5,6,41] It is also plausible that the stronger adsorption of +/pho JPs results in higher local concentrations of particles near the bilayer and thus a lower threshold concentration of particles needed to induce defects. Third, the bilayer remained fluidic even after defects were formed (Figure 5c). Lastly, −/pho JPs formed complexes with lipids extracted from the bilayer, as indicated by the colocalization between small lipid aggregates and fluorescently labeled −/pho JPs (Figure S8). However, these complexes were seen floating in the solution instead of remaining on the bilayer as for the +/pho JPs. This again shows that charges play an important role in particle adhesion to the bilayer. However, amphiphilic JPs, regardless of their charge, disrupt the bilayer in the same way by extracting lipids and inducing defects.

In order to understand the effects of particle hydrophobicity, we created three types of control particles: dipolar JPs displaying amine groups on one hemisphere and carboxylic acid groups on the other (referred to as +/− JPs) and particles functionalized uniformly with either amine (+UPs) or

DOI: 10.1021/acsnano.8b00759
ACS Nano 2018, 12, 3646−3657

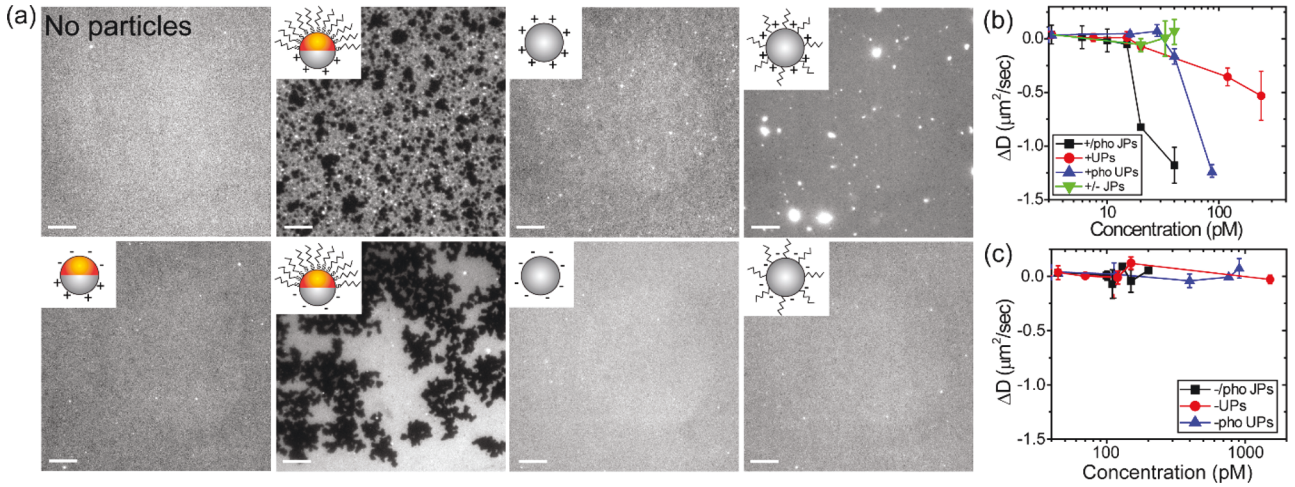

Figure 5. (a) Fluorescence images showing morphology of lipid bilayers at 70 min after interaction with different types of particles as indicated in the schematic inset. Concentration of particles was [+/pho JPs] = 40 pM; [+UPs] = 40 pM; [+pho UPs] = 40 pM; [+/− JPs] = 40 pM; [−/pho JPs] = 150 pM; [−UPs] = 150 pM; [−pho UPs] = 150 pM. (b and c) Change in lipid diffusion coefficient (ΔD) after the addition of different types of particles as a function of concentration. Scale bars: 10 μm.

carboxylic acid groups (−UPs). None of these three particle types induced visible defects in the bilayer even at particle concentrations as high as 240 pM (Figures 5a and S7). This makes it clear that the hydrophobicity of particles is required for inducing defects in lipid bilayers. This conclusion is consistent with our earlier observation that the hydrophobic hemispheres of +/pho JPs preferentially faced the bilayer after the formation of membrane defects. Among the three types of control particles, only +UPs adsorbed onto the lipid bilayer and caused a slight decrease in membrane fluidity (Figure 5b,c). This observation provides further evidence that cationic charges enhance particle adhesion onto bilayers, whereas anionic charges do not.

To determine the role of Janus geometry in particle−bilayer interactions, we created control particles that were coated uniformly with either a mixture of amine and hydrophobic groups (+pho UP) or a mixture of carboxylic acid and hydrophobic groups (−pho UP). The hydrophobic groups on these uniform particles have the same octadecyl alkyl structure as those on Janus particles. Comparing +pho UPs to +/pho JPs, we observed the appearance of small lipid−particle complexes at 30 pM and higher concentrations of +pho UPs, but no defects in the bilayer were seen even when particle concentration was increased to 90 pM (Figures 5a and S7). We could not test whether +pho UPs would induce defects in the bilayer at even higher concentrations because they aggregated severely beyond 90 pM. This result is in sharp contrast to the observation that +/pho JPs at 20 pM caused formation of lipid−particle complexes and extensive defects in bilayers (Figure 1c). Membrane fluidity decreased at 50 pM concentrations of +pho UP, as opposed to 20 pM for +/pho JPs. It is evident that +/pho JPs disrupt DOPC bilayers more effectively than +pho UPs. A similar conclusion was also drawn for −/pho JPs compared with −pho UPs. The −pho UPs did not induce any changes in either the morphology or the fluidity of the bilayer even at a particle concentration of 1.2 nM (Figures 5c and S7). Neither −/pho JPs or −pho UPs adhered to lipid bilayers. On the basis of these results, we conclude that Janus geometry enhances the membrane disruption caused by amphiphilic particles, regardless of the cationic or anionic charges on the other hemisphere. This effect might be related to the influence of Janus geometry on the adsorption of particles onto bilayers. We found that most +pho UPs remained floating in solution, whereas +/pho JPs adsorbed strongly onto lipid bilayers. This observation agrees with the predictions of computer simulations that repulsion between hydrophobic alkyl chains and polar lipid headgroups creates an energy barrier unfavorable for initial contact between a particle and a bilayer.[27] Importantly, our results here demonstrate that this repulsive force has a smaller effect on the adsorption of Janus particles than on the adsorption of uniform particles. Our findings about the orientation of +/pho JPs (Figure 4) make it plausible that for Janus particles with hydrophobic alkyl chains and charged groups on opposite hemispheres their freedom of rotation allows them to reorient for preferable particle−bilayer interactions in different situations.

In order to provide quantitative evidence for the argument given above, we measured the association constant (K_a) and activation energy (E_a) of particle adsorption on bilayers. Following a method reported previously,[42] we measured the surface density of nanoparticles adsorbed onto DOPC bilayers as a function of time, and from these plots we calculated K_a and E_a based on an assumption of classical collision theory (Table 1 and Figure S9). Our results show that the association constant of +/pho JPs (24 700 ± 180 M^{-1} s^{-1}) is significantly higher than that of +UPs (2280 ± 30 M^{-1} s^{-1}) or + pho UPs (119 ± 21 M^{-1} s^{-1}). Correspondingly, E_a (+/pho JPs) < E_a (+UPs) < E_a (+pho UPs). Two important conclusions can be drawn from these results. First, a uniform coating of hydrophobic alkyl chains hinders the initial attraction between cationic charges on particles and lipids. This is consistent with our experimental observations. Second, Janus geometry enhances the binding of

Table 1. Association Constant (K_a) and Activation Energy (E_a) of the Adsorption of Different Types of Particles on DOPC Lipid Bilayers

	K_a (M^{-1} s^{-1})	E_a (kJ/mol)
+/pho JPs	24 700 ± 180	43.3 ± 0.02
+UPs	2280 ± 30	49.2 ± 0.03
+pho UPs	119 ± 21	56.5 ± 0.4

DOI: 10.1021/acsnano.8b00759
ACS Nano 2018, 12, 3646−3657

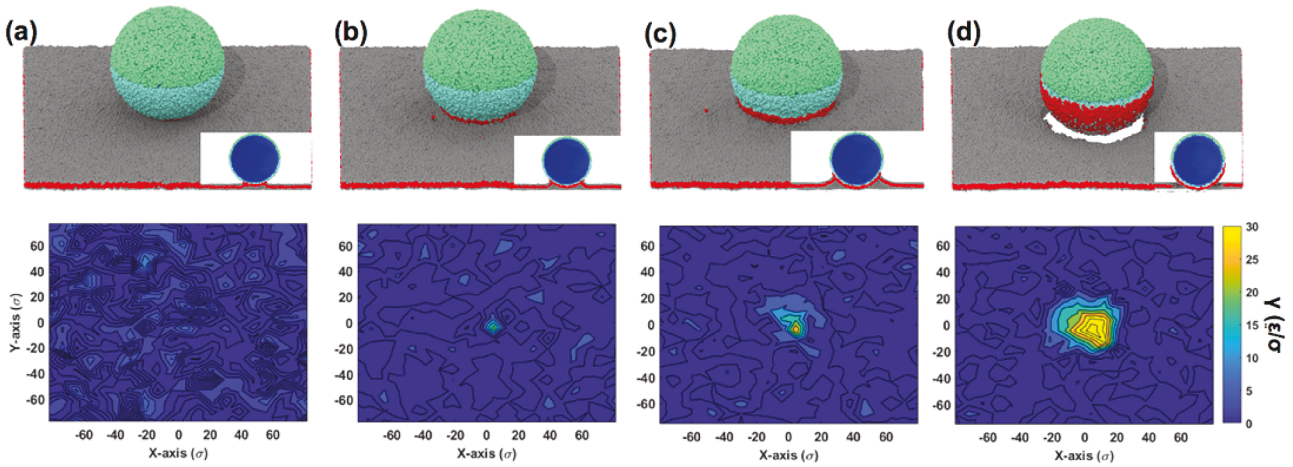

Figure 6. Computer simulation of the disruption of a lipid bilayer induced by an amphiphilic Janus nanoparticle. The hydrophilic and hydrophobic hemispheres of the Janus particle are shown in green and blue, respectively. (Top) Images showing the formation of the lipid–particle complex and defect. Insets are side views of the system. (Bottom) Spatial distribution of membrane tension (γ) corresponding to different stages in the bilayer rupture process.

amphiphilic particles to the bilayer. The strong binding of +/pho JPs to bilayers is consistent with our observation that they are more effective in inducing bilayer defects than other types of particles. Binding affinity for anionic particles was not quantified because they showed negligible adsorption on bilayers.

Lastly, we performed computer simulations to understand the mechanism by which amphiphilic Janus nanoparticles disrupt the bilayer after adsorption. The simulation model was developed based on our previous work.[43] Each Janus nanoparticle contains a spherical hard core, charged beads, and hydrophobic beads coating its core surface (Figure S10). The Deserno–Cooke solvent-free model for lipid bilayers is applied based on an attractive potential. The mass, length, and time scales are all normalized in the simulation, with the unit of length taken to be σ = 1 nm, the unit of mass to be that of the lipid beads m, and the unit of energy to be $\varepsilon = k_BT/1.1 = 2.2$ kJ/mol. All other quantities are expressed in terms of these basic units. At the beginning of the simulation, amphiphilic lipid molecules self-assemble into a bilayer membrane. In order to mimic our experimental system of a supported lipid bilayer confined on a glass substrate, the center of mass of the bilayer membrane is fixed to its original equilibrium position. It is noteworthy to point out that the simulation has a limited time scale compared to that of the experiments and is not capable of mimicking the entire dynamic process of nanoparticle attaching and detaching on the lipid membrane. To simulate the hydrophobic interaction between the Janus nanoparticle and the bilayer membrane, the Janus particle is initially positioned 5σ above the bilayer membrane with the hydrophobic hemisphere oriented toward the bilayer. As the simulation goes on, the particle approaches the bilayer to adsorb. Due to strong attraction between the hydrophobic tails of the lipids and the hydrophobic hemisphere of the particle, lipids can be extracted from the bilayer and diffuse onto the hydrophobic hemisphere. As shown in Figure 6, the gradual extraction of lipids leads to the loss of bilayer integrity and an eventual rupture of the bilayer membrane. From a mechanical viewpoint, the bilayer undergoes an irreversible deformation due to its strong interaction with the Janus particle. As the deformation reaches a critical point, the bilayer membrane starts to rupture as shown in Figure 6d.

To quantitatively explain the rupture of the bilayer membrane, the evolution of membrane tension during the interaction process was examined (the bottom panel in Figure 6). The surface tension for a surface normal in the z-direction inside a cell membrane is characterized by the pressure tensor P using the following relation:[44]

$$\gamma = \int_{Z_1}^{Z_2} [P_N(Z) - P_T(Z)]\, dZ$$

in which γ is the surface tension, P_N is the pressure normal to the bilayer surface, and P_T is the tangential pressure along the bilayer surface. For MD simulations, this equation can be further simplified:[45]

$$\gamma = L_Z[P_Z - (P_X + P_Y)/2]$$

In this equation, L_Z is the size of the simulation cell in the z-direction normal to the bilayer surface and P_i is the pressure in the $i = x, y, z$ direction. The bilayer membrane is initially in an equilibrium tensionless state, achieved by adjusting the simulation box size. As the particle–bilayer interaction proceeds, the membrane tension near the particle–bilayer contact area can reach up to $5\epsilon/\sigma$ to $15\epsilon/\sigma$ (which corresponds to 18 182–54 546 pN/μm in physical units), while the rest of the bilayer membrane away from the contact area almost remains as its original tensionless state. Our simulation results agree with previously reported experimental studies that a lipid bilayer ruptures when its surface area expands by ~3–5% compared to its relaxed state and the membrane tension reaches ~3000–10 000 pN/μm, indicating that particle-induced local deformation in our simulation is large enough to rupture the lipid membrane.[46]

Control simulations with uniform cationic and uniform hydrophobic nanoparticles were performed with the same parameter settings as for the amphiphilic Janus nanoparticles (Figures S11, S12). Simulations show that uniform hydrophobic particles rupture the lipid membrane, but uniform cationic ones do not. These results agree with our experimental findings that hydrophobic interaction is the driving force for lipid extraction in zwitterionic lipid bilayers. It is important to point out that the simulation result on uniform hydrophobic particles cannot be experimentally validated, because such

DOI: 10.1021/acsnano.8b00759
ACS Nano 2018, 12, 3646–3657

particles aggregate severely in aqueous solution. In addition, the simulation, due to its limited time scale, is only focused on the membrane rupture stage instead of the entire process of particle−membrane interaction.

On the basis of all the results presented here, we propose the following mechanism for the interaction between amphiphilic Janus nanoparticles and zwitterionic lipid bilayers. (i) Initial contact between particles and bilayer membranes is driven by the attraction between the charges on particles and dipolar lipid head groups. The attraction is stronger for cationic charges. As a result, +/pho JPs adsorb strongly, whereas −/pho JPs only make transient contact with the bilayer. (ii) Disruption of the bilayer is driven by interaction between the hydrophobic hemisphere of the particle and the alkyl tails of the lipids. Amphiphilic Janus particles rotate to expose their hydrophobic hemisphere to the bilayer after the initial contact. The hydrophobic attraction leads to the extraction of lipids from the bilayer membrane. These lipids form complexes with the nanoparticles by adsorbing on their hydrophobic hemispheres. As the particle concentration increases, the gradual loss of lipids causes the membrane tension to increase beyond a threshold at which the membrane ruptures to form holes.

CONCLUSIONS

In this study, we investigated the mechanism by which amphiphilic Janus nanoparticles disrupt zwitterionic DOPC lipid bilayers and identified the different roles played by Janus geometry, hydrophobicity, and charge in the particle−bilayer interactions. We did this by using Janus particles with a well-defined anisotropic arrangement of functional groups on their surfaces. Our results demonstrate that hydrophobicity is required for amphiphilic Janus nanoparticles to extract lipids from the lipid bilayer and thereby create holes, whereas cationic charges promote the initial adhesion of particles onto the bilayer. We showed that 100 nm amphiphilic Janus nanoparticles, whether cationic or anionic on one hemisphere, disrupt lipid bilayers more effectively than particles that are coated uniformly with the same chemical groups. Such efficiency is a result of the spatial segregation of the hydrophobic and charged groups. Janus particles, unlike their uniformly coated counterparts, can reorient to interact with the bilayer from a hemisphere with preferred chemistry. On the basis of these results, we can now explore in future studies many interesting questions, such as the interplay between the anisotropic surface chemistry and size of nanoparticles. Compared to the extensive studies on nanoparticles with uniform surface coatings, this study provides an understanding of a scarcely explored question: how does heterogeneous surface chemistry change the biological behavior of nanoparticles? More importantly, the findings presented here underscore the importance of the spatial organization of molecules in determining the interactions between nanoparticles and biological systems. There is currently intense research interest in synthesizing amphiphilic nanoparticles for a variety of practical applications.[47−52] Broadly speaking, our study provides insights for understanding the biological impact of such particles and the possibility of using the surface anisotropy of Janus nanoparticles to tailor-make particle−membrane hybrid structures.

EXPERIMENTAL AND COMPUTER SIMULATION METHODS

Materials. Amine-functionalized silica particles (100 nm) were purchased from Nanocomposix (San Diego, CA, USA). Octadecanethiol, cysteamine hydrochloride, catalase from bovine liver, and glucose oxidase from *Aspergillus niger* were obtained from Sigma-Aldrich (St. Louis, MO, USA). Mercaptoundecanoic acid was procured from Santa Cruz Biotechnology (Santa Cruz, CA, USA). Octadecyltrimethoxysilane was purchased from Gelest Inc. (Morrisville, PA, USA). Chromium (99.99% purity) and gold (99.99% purity) pellets were purchased from Kurt J. Lesker (Jefferson Hills, PA, USA). Cyanine5 *N*-hydroxysuccinimide ester (Cy5 NHS ester) was procured from Lumiprobe Corporation (Hunt Valley, MD, USA). Succinic anhydride (99% GC) was purchased from AK Scientific, Inc. (Union City, CA, USA). Phospholipids, 1,2-dioleoyl-*sn*-glycero-3-phosphocholine (DOPC) and 1,2-dipalmitoyl-*sn*-glycero-3-phosphoethanolamine-*N*-lissamine rhodamine B sulfonyl (RhB-PE), were purchased from Avanti Polar Lipid (Alabaster, AL, USA). *N*-(4,4-Difluoro-5,7-dimethyl-4-bora-3a,4a-diaza-*s*-indacene-3-propionyl)-1,2-dihexadecanoyl-*sn*-glycero-3-phosphoethanolamine, triethylammonium salt (BODIPY-DHPE) was purchased from Thermo Scientific (Waltham, MA, USA). Bovine serum albumin conjugated with Alexa Fluor 647 was attained from Thermo Scientific. Toluene was purchased from Avantor Performance Materials, LLC (Center Valley, PA, USA). Ultrapure water (resistivity of 18.2 MΩ·cm) was used for all experiments.

Fabrication of Particles. Submonolayers of amine-functionalized silica nanoparticles were prepared using the solvent evaporation method with modification.[53] Briefly, 50 μL of 0.1 wt % particles in ethanol was applied on a piranha-etched glass microscope slide. A continuous gentle stream of filtered air was applied during solvent evaporation to reduce the coffee-stain effect. The submonolayers of particles were coated sequentially with layers of chromium (5 nm) and then gold (25 nm) using an Edward Thermal evaporator (Nanoscale Characterization Facility at Indiana University). Immediately after the metal deposition, the microscope slides were immersed and stored in ethanol containing 2 mM ODT until use. Particles were removed from microscope slides *via* sonication in ethanol only prior to experiments in order to prevent particle aggregation. Particle aggregates were further removed by differential centrifugation three times at 100 rcf for 30 s each and then three times at 500 rcf for 30 s each. Particles were washed and redispersed in water immediately before being added to supported lipid bilayers. For preparing anionic amphiphilic Janus nanoparticles (−/pho JPs), amine groups on silica particles were converted to carboxylic acids using succinic anhydride.[54] In the experiment, 250 μL of amine-functionalized silica particles (1 mg/mL in dimethylformamide, DMF) was added dropwise into 5 mL of DMF containing 0.1 M succinic anhydride. The reaction was kept at room temperature for 20 h. After the reaction, particles were washed with DMF and then ethanol and stored in DMF until further use. For preparing amphiphilic uniform particles, OTE was mixed in chloroform (OTE/chloroform = 1:5 v/v) for surface functionalization. Glass vials to be used for particle functionalization were first treated with OTE on the interior surface. A 100 μL amount of OTE chloroform solution was added to 2 mL of amine-functionalized silica particles (0.5 mg/mL in ethanol) under stirring, and 30 μL of NH_4OH (28−30 wt %) was added subsequently. The reaction was kept at room temperature for 24 h. Particles after functionalization were washed with ethanol, water, and ethanol sequentially and stored in ethanol until use. To fluorescently label particles, Cy5 dissolved in DMSO (0.5 mg/mL) was added to amine-functionalized particles dispersed in 1× phosphate-buffered saline (PBS) (pH 7.4) for reaction overnight at room temperature. The final concentration of Cy5 was 0.8 μM, and particle concentration was 80 pM. After the reaction, particles were washed with water and stored in the ethanol.

Characterization of Particles. Hydrodynamic size and zeta potential of particles were measured in deionized water with a Zetasizer. The morphology of Janus particles was characterized using SEM. The concentration of Janus particles was measured with a

DOI: 10.1021/acsnano.8b00759
ACS Nano 2018, 12, 3646−3657

ZetaView nanoparticle tracking analyzer. Amphiphilicity of particles was confirmed using the phase transfer method.[55] Briefly, particles dispersed in 100 μL of water were added to a vial containing 200 μL of toluene and 100 μL of water. After the mixed solution was vortexed gently and then kept still for 5 min, the dispersion of Janus particles at the toluene−water interface or in the bulk liquid phases was examined.

Preparation of Supported Lipid Bilayers. To first prepare unilamellar vesicles (diameter of 100 nm), DOPC and fluorescent lipids, either BODIPY-DHPE or Rhd-DHPE, were mixed in chloroform at 500:1 molar ratio and dried in a round-bottom flask under nitrogen flow. Dried lipid films were hydrated in 1× PBS to a final lipid concentration of 1 mg/mL. The lipid solution was vortexed and underwent freeze-and-thaw cycles five times before being extruded through a 100 nm filter membrane using a mini-extruder. To prepare the supported lipid bilayer using the vesicle fusion method, lipid vesicles were diluted with water to a final concentration of 0.2 mg/mL and immediately added to a precleaned glass-bottom imaging chamber. After incubation for 1 h, the formation of lipid bilayer was complete, and excess lipid vesicles were rinsed away with water thoroughly.

Fluorescence Imaging. Wide-field epi-fluorescence imaging of lipid bilayers and particles was done using a Nikon Eclipse Ti microscope equipped with an Andor iXon3 EMCCD Camera and a Nikon Plan Apo 100×/1.49 NA TIRF objective. Each experiment was repeated twice on at least two different days to ensure reproducibility. All experiments were done at room temperature unless indicated otherwise. In experiments of increased temperature, particles were rinsed away from the bilayer after defect formation was confirmed. The temperature of the imaging chamber was raised gradually from room temperature to 27, 37, 47, and 57 °C. The temperature was allowed to stabilize for 3 min before fluorescence images were acquired. In BSA backfilling experiments, particles were rinsed away after defect formation was confirmed. Subsequently, BSA was incubated with the lipid bilayer at a final concentration of 0.75 μM for 15 min before rinsing and imaging. BSA backfilling samples for STORM imaging were prepared in a reducing buffer that enhances Alexa 647 blinking. The reducing buffer contained 9.8% glucose (m/v), 9.8 mM NaCl, 49 mM Tris-HCl (pH 8.0), 6.8 mM cysteamine hydrochloride, 160 pM of catalase, and 0.14 mg of glucose oxidase in 200 μL of deionized water. The buffer was filtered through a 0.2 μm membrane filter for sterilization and used fresh prior to each imaging.

STORM imaging was done using an OMX Super-Resolution system equipped with a Photometrics Cascade II EMCCD camera and an Olympus UAPO N 100×/1.49 NA TIRF objective. All images were acquired with a continuous illumination at 642 nm following an activation 1 ms pulse of 405 nm excitation. At each field of view, 50 000 frames were taken in "localization" mode and processed with SoftWoRx software (Applied Precision) to obtain super-resolution images.

Fluorescence Recovery after Photobleaching. FRAP measurement of lipid diffusion was conducted in the epi-fluorescence imaging configuration using a Nikon Eclipse Ti microscope. A circular region of the bilayer in the field of view was photobleached using a 488 nm laser, and the recovery of fluorescence was recorded every 2 s until 240 s after photobleaching. For each sample, FRAP was measured before and 80 min after the addition of particles. An ImageJ (NIH) plugin "simFRAP" was used for image processing. It computes a diffusion coefficient based on fitting a computer-simulated recovery profile to experimental FRAP data. An advantage of this program is that the calculation of the diffusion coefficient does not depend on the photobleaching geometry.[56]

Quantification of Janus Particle Orientation. Silicon wafers (for SEM) and glass microscope slides (for fluorescence imaging) were etched with piranha solution (H_2SO_4/H_2O_2 = 3:1 v/v for 15 min and used as hydrophilic substrates. To fabricate hydrophobic substrates, silicon wafers and glass microscope slides were immersed in a mixture solution that was made by mixing 100 μL of OTE/chloroform (1:5 v/v) solution with 2 mL of enthanol. After 24 h of reaction, the silicon wafers were washed with ethanol three times and stored in water. The water contact angle was measured to be less than 5° on the piranha-etched silicon wafers and 77 ± 2° on the OTE-coated ones. To prepare the calibration samples, +/pho JPs were casted on different substrates and dried while swirling using a pipet tip to reduce the coffee-stain effect. Particles were imaged using SEM to obtain their orientation and epi-fluorescence microscopy to measure their intensity of emission.

Measurement of Particle−Bilayer Binding Constant. This measurement follows a previously reported method based on a classical collision theory between nanoparticles and surface.[42] Briefly, adsorption and desorption of Cy5-labeled particles on lipid bilayers were imaged using epi-fluorescence microscopy. The number of adsorbed particles per unit surface area (N) was counted using a single-particle tracking Matlab algorithm and plotted against elapsed time (t) after the addition of particles. After a linear fit, the slope of the fit was obtained as the overall adsorption rate, dN/dt. By simplifying the particle−bilayer binding as a second-order ligand/receptor association process, dN/dt can be expressed as

$$\frac{dN}{dt} = K_a C_s C_n \tag{1}$$

in which K_a is the association constant, C_s is the maximum number of binding sites on the bilayer, and C_n is the bulk concentration of the nanoparticles. C_s was calculated to be 115 assuming a close packing of nanoparticles (d = 100 nm) on a flat surface. K_a was calculated based on the obtained values of C_s, dN/dt, and C_n.

The activation energy for particle−bilayer binding was calculated using the following equation:

$$E_a = [\ln(Q) - \ln(k_a)]k_B T \tag{2}$$

in which Q is the diffusion collision frequency factor, k_B is the Boltzmann constant, and T is temperature. Q was estimated based on the following equation, assuming that the association is limited by the diffusion of nanoparticles:

$$Q \approx 2000\pi R D N_a \tag{3}$$

in which R is the radius of the nanoparticles, D is the diffusion constant of particles in solution, and N_a is Avogadro's number. D can be calculated based on the Stokes−Einstein equation:

$$D = \frac{k_B T}{6\pi\eta r} \tag{4}$$

Q for our system was estimated to be 9.285×10^{11} M^{-1} s^{-1}.

Computer Simulation. The simulation box (Figure S10) contains 158 436 beads forming a bilayer membrane and 22 620 beads forming the Janus nanoparticle (NP). The Janus NP consists of 5655 beads (N) forming a spherical NP core, 8481 charged beads (C, + 0.1e), and 8484 hydrophobic beads (P) coating the NP core surface. The Deserno−Cooke solvent-free model for lipid bilayers is applied based on an attractive potential, which can help reduce simulation time up to 90% compared to a model with explicit solvents. The solvent-mediated interaction between lipid tails is represented by an effective attractive potential of a sufficiently broad range. This solvent-free model has been widely used to investigate the interaction between nanoparticles and cell membranes.[57,58] Periodic boundary conditions are applied in three directions of the simulation box. The mass, length, and time scales are all normalized in the simulations, with the unit of length taken to be σ = 1 nm, the unit of mass to be that of the lipid beads m, and the unit of energy to be $\varepsilon = k_B T/1.1$ = 2.2 kJ/mol. All other quantities are expressed in terms of these basic units. We use a velocity-Verlet algorithm to perform time integration and a Langevin thermostat to control the system temperature, T. The integration time step is Δt = 0.01 τ where τ is 15 ns. All simulations are performed with LAMMPS package.[59]

Each lipid molecule in the computational model is represented by one head bead (H) followed by two tail beads (T). The size of a lipid is fixed *via* a Weeks−Chandler−Andersen potential:

$$U_{WCA} = 4\epsilon\left[\left(\frac{b}{r_{ij}}\right)^{12} - \left(\frac{b}{r_{ij}}\right)^{6} + \frac{1}{4}\right], r_{ij} < r_c = \sqrt[6]{2}\,b \tag{5}$$

DOI: 10.1021/acsnano.8b00759
ACS Nano 2018, 12, 3646−3657

where ϵ is the depth of the potential well, b is the finite distance at which the interparticle potential is zero, and r_{ij} is the distance between the particles. In order to ensure the cylindrical lipid shape, b is set as $b_{head,head} = b_{head,tail} = 0.95\sigma$ and $b_{tail,tail} = \sigma$. The three beads in a single lipid are linked by two FENE bonds:

$$U_{FENE} = \sum_{bonds} -\frac{1}{2}k_{fene}R_{max}^2 \ln\left(1 - \frac{r_{ij}^2}{R_{max}^2}\right) \quad (6)$$

with the stiffness $k_{fene} = 30\varepsilon/\sigma^2$ and the divergence length $R_{max} = 1.5\sigma$. Lipids are straightened by a harmonic spring:

$$U_{stretching} = \sum_{bonds} k_{stretch}(r_{ij} - r_0)^2 \quad (7)$$

with the bending stiffness $k_{stretch} = 10\varepsilon/\sigma^2$ and the equilibrium length $r_0 = 4\sigma$ between the head bead and the second tail bead. The ligand beads are also connected with a harmonic spring with $k_{stretch} = 100\varepsilon/\sigma^2$ and equilibrium length $r_0 = 1\sigma$. The hydrophobic effect is compensated by an attractive interaction between the tail beads as

$$U_{cos} = \begin{cases} -\epsilon, & r_{ij} < r_c \\ -\epsilon \cos^2[\pi(r_{ij} - r_c)/2w], & r_c \le r_{ij} \le r_c + w \\ 0, & r_{ij} > r_c + w \end{cases} \quad (8)$$

which describes an attractive potential with depth ε that smoothly tapers to zero for $r > r_c$. In our case, the decay range w is set as 1.6σ. Electrostatic interaction between any two charged beads with charge value q_i and q_j is given by the Coulomb potential

$$U_{Coul} = \frac{Gq_iq_j}{\varepsilon_0 r_{ij}} \quad (9)$$

where G is an energy-conversion constant and ε_0 is the dielectric constant. The particle−particle particle-mesh method is used to calculate the electrostatic interactions. The interaction between other beads is described by the Lennard-Jones potential function

$$U_{LJ} = 4\epsilon\left[\left(\frac{b}{r_{ij}}\right)^{12} - \left(\frac{b}{r_{ij}}\right)^{6}\right], r_{ij} < r_c = 2.5\sigma \quad (10)$$

where ϵ and b are the depth of the potential well and the finite distance at which the interbead potential is zero, respectively. All the important parameters for the bilayer membrane and coated NPs are listed in Table S1. Control simulations of particles with a uniform hydrophobic or cationic hydrophilic coating were performed with the same parameter setting as for Janus NPs.

ASSOCIATED CONTENT

Supporting Information

The Supporting Information is available free of charge on the ACS Publications website at DOI: 10.1021/acsnano.8b00759.

Figures S1−S12 and Table S1 (PDF)

Movie S1 (AVI)

AUTHOR INFORMATION

Corresponding Author

*E-mail (Y. Yu): yy33@indiana.edu.

ORCID

Xianqiao Wang: 0000-0003-2461-3015

Yan Yu: 0000-0001-6496-5045

Notes

The authors declare no competing financial interest.

ACKNOWLEDGMENTS

We thank Dr. Giovanni Gonzalez-Gutierrez at IUB Physical Biochemistry Instrumentation Facility and Dr. Jim Powers at IUB Light Microscopy Imaging Center for assistance with instrument use. Fabrication and characterization of Janus particles were done at the IUB Nanoscale Characterization Facility. This work was supported by the National Science Foundation under Grant No. 1705384 to Y.Y.

REFERENCES

(1) Chen, J. M.; Hessler, J. A.; Putchakayala, K.; Panama, B. K.; Khan, D. P.; Hong, S.; Mullen, D. G.; DiMaggio, S. C.; Som, A.; Tew, G. N.; Lopatin, A. N.; Baker, J. R.; Holl, M. M. B.; Orr, B. G. Cationic Nanoparticles Induce Nanoscale Disruption in Living Cell Plasma Membranes. *J. Phys. Chem. B* **2009**, *113*, 11179−11185.

(2) Cho, E. C.; Xie, J. W.; Wurm, P. A.; Xia, Y. N. Understanding the Role of Surface Charges in Cellular Adsorption *versus* Internalization by Selectively Removing Gold Nanoparticles on the Cell Surface with a I-2/KI Etchant. *Nano Lett.* **2009**, *9*, 1080−1084.

(3) Arvizo, R. R.; Miranda, O. R.; Thompson, M. A.; Pabelick, C. M.; Bhattacharya, R.; Robertson, J. D.; Rotello, V. M.; Prakash, Y. S.; Mukherjee, P. Effect of Nanoparticle Surface Charge at the Plasma Membrane and Beyond. *Nano Lett.* **2010**, *10*, 2543−2548.

(4) Harush-Frenkel, O.; Rozentur, E.; Benita, S.; Altschuler, Y. Surface Charge of Nanoparticles Determines Their Endocytic and Transcytotic Pathway in Polarized MDCK Cells. *Biomacromolecules* **2008**, *9*, 435−443.

(5) Hong, S. P.; Bielinska, A. U.; Mecke, A.; Keszler, B.; Beals, J. L.; Shi, X. Y.; Balogh, L.; Orr, B. G.; Baker, J. R.; Holl, M. M. B. Interaction of Poly(amidoamine) Dendrimers with Supported Lipid Bilayers and Cells: Hole Formation and the Relation to Transport. *Bioconjugate Chem.* **2004**, *15*, 774−782.

(6) Lin, J. Q.; Zhang, H. W.; Chen, Z.; Zheng, Y. G. Penetration of Lipid Membranes by Gold Nanoparticles: Insights into Cellular Uptake, Cytotoxicity, and Their Relationship. *ACS Nano* **2010**, *4*, 5421−5429.

(7) Tatur, S.; Maccarini, M.; Barker, R.; Nelson, A.; Fragneto, G. Effect of Functionalized Gold Nanoparticles on Floating Lipid Bilayers. *Langmuir* **2013**, *29*, 6606−6614.

(8) Ginzburg, V. V.; Balijepailli, S. Modeling the Thermodynamics of the Interaction of Nanoparticles with Cell Membranes. *Nano Lett.* **2007**, *7*, 3716−3722.

(9) Jing, B. X.; Zhu, Y. X. Disruption of Supported Lipid Bilayers by Semihydrophobic Nanoparticles. *J. Am. Chem. Soc.* **2011**, *133*, 10983−10989.

(10) Van Lehn, R. C.; Ricci, M.; Silva, P. H. J.; Andreozzi, P.; Reguera, J.; Voitchovsky, K.; Stellacci, F.; Alexander-Katz, A. Lipid Tail Protrusions Mediate the Insertion of Nanoparticles into Model Cell Membranes. *Nat. Commun.* **2014**, *5*, 4482.

(11) Lee, H. Y.; Shin, S. H. R.; Abezgauz, L.; Lewis, S. A.; Chirsan, A. M.; Danino, D.; Bishop, K. J. M. Integration of Gold Nanoparticles into Bilayer Structures *via* Adaptive Surface Chemistry. *J. Am. Chem. Soc.* **2013**, *135*, 12476−12476.

(12) Gao, J. H.; Zhang, O.; Ren, J.; Wu, C. L.; Zhao, Y. B. Aromaticity/Bulkiness of Surface Ligands to Promote the Interaction of Anionic Amphiphilic Gold Nanoparticles with Lipid Bilayers. *Langmuir* **2016**, *32*, 1601−1610.

(13) Pogodin, S.; Werner, M.; Sommer, J. U.; Baulin, V. A. Nanoparticle-Induced Permeability of Lipid Membranes. *ACS Nano* **2012**, *6*, 10555−10561.

(14) Moyano, D. F.; Saha, K.; Prakash, G.; Yan, B.; Kong, H.; Yazdani, M.; Rotello, V. M. Fabrication of Corona-Free Nanoparticles with Tunable Hydrophobicity. *ACS Nano* **2014**, *8*, 6748−6755.

(15) Saha, K.; Rahimi, M.; Yazdani, M.; Kim, S. T.; Moyano, D. F.; Hou, S.; Das, R.; Mout, R.; Rezaee, F.; Mahmoudi, M.; Rotello, V. M. Regulation of Macrophage Recognition through the Interplay of Nanoparticle Surface Functionality and Protein Corona. *ACS Nano* **2016**, *10*, 4421−4430.

DOI: 10.1021/acsnano.8b00759
ACS Nano 2018, 12, 3646−3657

(16) Saha, K.; Moyano, D. F.; Rotello, V. M. Protein Coronas Suppress the Hemolytic Activity of Hydrophilic and Hydrophobic Nanoparticles. *Mater. Horiz.* **2014**, *1*, 102−105.
(17) Walkey, C. D.; Olsen, J. B.; Song, F. Y.; Liu, R.; Guo, H. B.; Olsen, D. W. H.; Cohen, Y.; Emili, A.; Chan, W. C. W. Protein Corona Fingerprinting Predicts the Cellular Interaction of Gold and Silver Nanoparticles. *ACS Nano* **2014**, *8*, 2439−2455.
(18) Lesniak, A.; Fenaroli, F.; Monopoli, M. R.; Aberg, C.; Dawson, K. A.; Salvati, A. Effects of the Presence or Absence of a Protein Corona on Silica Nanoparticle Uptake and Impact on Cells. *ACS Nano* **2012**, *6*, 5845−5857.
(19) Tenzer, S.; Docter, D.; Kuharev, J.; Musyanovych, A.; Fetz, V.; Hecht, R.; Schlenk, F.; Fischer, D.; Kiouptsi, K.; Reinhardt, C.; Landfester, K.; Schild, H.; Maskos, M.; Knauer, S. K.; Stauber, R. H. Rapid Formation of Plasma Protein Corona Critically Affects Nanoparticle Pathophysiology. *Nat. Nanotechnol.* **2013**, *8*, 772−781.
(20) Jing, B. X.; Abot, R. C. T.; Zhu, Y. X. Semihydrophobic Nanoparticle-Induced Disruption of Supported Lipid Bilayers: Specific Ion Effect. *J. Phys. Chem. B* **2014**, *118*, 13175−13182.
(21) Shin, S. H.; Lee, H. Y.; Bishop, K. J. Amphiphilic Nanoparticles Control the Growth and Stability of Lipid Bilayers with Open Edges. *Angew. Chem., Int. Ed.* **2015**, *54*, 10816−10820.
(22) Li, Y.; Zhang, X. R.; Cao, D. P. A Spontaneous Penetration Mechanism of Patterned Nanoparticles across a Biomembrane. *Soft Matter* **2014**, *10*, 6844−6856.
(23) Van Lehn, R. C.; Alexander-Katz, A. Free Energy Change for Insertion of Charged, Monolayer-Protected Nanoparticles into Lipid Bilayers. *Soft Matter* **2014**, *10*, 648−658.
(24) Li, Y. F.; Li, X. J.; Li, Z. H.; Gao, H. J. Surface-Structure-Regulated Penetration of Nanoparticles across a Cell Membrane. *Nanoscale* **2012**, *4*, 3768−3775.
(25) Van Lehn, R. C.; Alexander-Katz, A. Penetration of Lipid Bilayers by Nanoparticles with Environmentally-Responsive Surfaces: Simulations and Theory. *Soft Matter* **2011**, *7*, 11392−11404.
(26) Pogodin, S.; Slater, N. K. H.; Baulin, V. A. Biomolecule Surface Patterning May Enhance Membrane Association. *ACS Nano* **2012**, *6*, 1308−1313.
(27) Ding, H. M.; Ma, Y. Q. Interactions between Janus Particles and Membranes. *Nanoscale* **2012**, *4*, 1116−1122.
(28) Alexeev, A.; Uspal, W. E.; Balazs, A. C. Harnessing Janus Nanoparticles to Create Controllable Pores in Membranes. *ACS Nano* **2008**, *2*, 1117−1122.
(29) Salib, I.; Yong, X.; Crabb, E. J.; Moellers, N. M.; McFarlin, G. T.; Kuksenok, O.; Balazs, A. C. Harnessing Fluid-Driven Vesicles To Pick Up and Drop Off Janus Particles. *ACS Nano* **2013**, *7*, 1224−1238.
(30) Verma, A.; Uzun, O.; Hu, Y. H.; Hu, Y.; Han, H. S.; Watson, N.; Chen, S. L.; Irvine, D. J.; Stellacci, F. Surface-Structure-Regulated Cell-Membrane Penetration by Monolayer-Protected Nanoparticles. *Nat. Mater.* **2008**, *7*, 588−595.
(31) Van Lehn, R. C.; Atukorale, P. U.; Carney, R. P.; Yang, Y. S.; Stellacci, F.; Irvine, D. J.; Alexander-Katz, A. Effect of Particle Diameter and Surface Composition on the Spontaneous Fusion of Monolayer-Protected Gold Nanoparticles with Lipid Bilayers. *Nano Lett.* **2013**, *13*, 4060−4067.
(32) Stirling, J.; Lekkas, I.; Sweetman, A.; Djuranovic, P.; Guo, Q. M.; Pauw, B.; Granwehr, J.; Levy, R.; Moriarty, P. Critical Assessment of the Evidence for Striped Nanoparticles. *PLoS One* **2014**, *9*, e108482.
(33) Ong, Q. K.; Stellacci, F. Response to "Critical Assessment of the Evidence for Striped Nanoparticles". *PLoS One* **2015**, *10*, e0135594.
(34) Cesbron, Y.; Shaw, C. P.; Birchall, J. P.; Free, P.; Levy, R. Stripy Nanoparticles Revisited. *Small* **2012**, *8*, 3714−3719.
(35) Bazant, M. Z.; Squires, T. M. Induced-Charge Electrokinetic Phenomena. *Curr. Opin. Colloid Interface Sci.* **2010**, *15*, 203−213.
(36) Shi, J. J.; Chen, J. X.; Cremer, P. S. Sub-100 nm Patterning of Supported Bilayers by Nanoshaving Lithography. *J. Am. Chem. Soc.* **2008**, *130*, 2718−2719.
(37) Adams, P. G.; Swingle, K. L.; Paxton, W. F.; Nogan, J. J.; Stromberg, L. R.; Firestone, M. A.; Mukundan, H.; Montano, G. A. Exploiting Lipopolysaccharide-Induced Deformation of Lipid Bilayers to Modify Membrane Composition and Generate Two-Dimensional Geometric Membrane Array Patterns. *Sci. Rep.* **2015**, *5*, 10331.
(38) Roberts, T. G.; Anker, J. N.; Kopelman, R. Magnetically Modulated Optical Nanoprobes (MagMOONs) for Detection and Measurement of Biologically Important Ions against the Natural Background Fluorescence of Intracellular Environments. *J. Magn. Magn. Mater.* **2005**, *293*, 715−724.
(39) Anthony, S. M.; Hong, L.; Kim, M.; Granick, S. Single-Particle Colloid Tracking in Four Dimensions. *Langmuir* **2006**, *22*, 9812−9815.
(40) Hong, L.; Anthony, S. M.; Granick, S. Rotation in Suspension of a Rod-Shaped Colloid. *Langmuir* **2006**, *22*, 7128−7131.
(41) Leroueil, P. R.; Berry, S. A.; Duthie, K.; Han, G.; Rotello, V. M.; McNerny, D. Q.; Baker, J. R.; Orr, B. G.; Banaszak Holl, M. M. Wide Varieties of Cationic Nanoparticles Induce Defects in Supported Lipid Bilayers. *Nano Lett.* **2008**, *8*, 420−424.
(42) Wei, L.; Zhao, X.; Chen, B.; Li, H.; Xiao, L.; Yeung, E. S. Frozen Translational and Rotational Motion of Human Immunodeficiency Virus Transacting Activator of Transcription Peptide-Modified Nanocargo on Neutral Lipid Bilayer. *Anal. Chem.* **2013**, *85*, 5169−5175.
(43) Zhang, L.; Xu, B.; Wang, X. Cholesterol Extraction from Cell Membrane by Graphene Nanosheets: A Computational Study. *J. Phys. Chem. B* **2016**, *120*, 957−964.
(44) Simunovic, M.; Voth, G. A. Membrane Tension Controls the Assembly of Curvature-Generating Proteins. *Nat. Commun.* **2015**, *6*, 7219.
(45) Chiu, S. W.; Clark, M.; Balaji, V.; Subramaniam, S.; Scott, H. L.; Jakobsson, E. Incorporation of Surface Tension into Molecular Dynamics Simulation of an Interface: a Fluid Phase Lipid Bilayer Membrane. *Biophys. J.* **1995**, *69*, 1230−1245.
(46) Lieber, A. D.; Yehudai-Resheff, S.; Barnhart, E. L.; Theriot, J. A.; Keren, K. Membrane Tension in Rapidly Moving Cells Is Determined by Cytoskeletal Forces. *Curr. Biol.* **2013**, *23*, 1409−1417.
(47) Jiang, S.; Chen, Q.; Tripathy, M.; Luijten, E.; Schweizer, K. S.; Granick, S. Janus Particle Synthesis and Assembly. *Adv. Mater.* **2010**, *22*, 1060−1071.
(48) Hong, L.; Cacciuto, A.; Luijten, E.; Granick, S. Clusters of Charged Janus Spheres. *Nano Lett.* **2006**, *6*, 2510−2514.
(49) Hu, J.; Zhou, S. X.; Sun, Y. Y.; Fang, X. S.; Wu, L. M. Fabrication, Properties and Applications of Janus Particles. *Chem. Soc. Rev.* **2012**, *41*, 4356−4378.
(50) Gao, W.; Pei, A.; Feng, X. M.; Hennessy, C.; Wang, J. Organized Self-Assembly of Janus Micromotors with Hydrophobic Hemispheres. *J. Am. Chem. Soc.* **2013**, *135*, 998−1001.
(51) Chen, Q.; Yan, J.; Zhang, J.; Bae, S. C.; Granick, S. Janus and Multiblock Colloidal Particles. *Langmuir* **2012**, *28*, 13555−13561.
(52) Ren, B.; Ruditskiy, A.; Song, J. H.; Kretzschmar, I. Assembly Behavior of Iron Oxide-Capped Janus Particles in a Magnetic Field. *Langmuir* **2012**, *28*, 1149−1156.
(53) Lee, K.; Yu, Y. Janus Nanoparticles for T Cell Activation: Clustering Ligands to Enhance Stimulation. *J. Mater. Chem. B* **2017**, *5*, 4410−4415.
(54) An, Y.; Chen, M.; Xue, Q.; Liu, W. Preparation and Self-Assembly of Carboxylic Acid-Functionalized Silica. *J. Colloid Interface Sci.* **2007**, *311*, 507−13.
(55) Jiang, S.; Schultz, M. J.; Chen, Q.; Moore, J. S.; Granick, S. Solvent-Free Synthesis of Janus Colloidal Particles. *Langmuir* **2008**, *24*, 10073−7.
(56) Blumenthal, D.; Goldstien, L.; Edidin, M.; Gheber, L. A. Universal Approach to FRAP Analysis of Arbitrary Bleaching Patterns. *Sci. Rep.* **2015**, *5*, 11655.
(57) Lee, M. W.; Han, M.; Bossa, G. V.; Snell, C.; Song, Z.; Tang, H.; Yin, L.; Cheng, J.; May, S.; Luijten, E.; Wong, G. C. Interactions between Membranes and "Metaphilic" Polypeptide Architectures with Diverse Side-Chain Populations. *ACS Nano* **2017**, *11*, 2858−2871.
(58) Sun, J.; Zhang, L.; Wang, J.; Feng, Q.; Liu, D.; Yin, Q.; Xu, D.; Wei, Y.; Ding, B.; Shi, X.; Jiang, X. Tunable Rigidity of (Polymeric

DOI: 10.1021/acsnano.8b00759
ACS Nano 2018, 12, 3646−3657

Core)−(Lipid Shell) Nanoparticles for Regulated Cellular Uptake. *Adv. Mater.* **2015**, *27*, 1402−1407.
(59) Plimpton, S. Fast Parallel Algorithms for Short-Range Molecular Dynamics. *J. Comput. Phys.* **1995**, *117*, 1−19.

DOI: 10.1021/acsnano.8b00759
ACS Nano 2018, 12, 3646−3657